

First-order antiferromagnetic transitions of SrMn₂P₂ and CaMn₂P₂ single crystals containing corrugated-honeycomb Mn sublattices

N. S. Sangeetha^{a,1}, Santanu Pakhira^a, Qing-Ping Ding^{a,b}, Lennard Krause^{c,d}, Hyung-Cheol Lee^{a,b}, Volodymyr Smetana^e, Anja-Verena Mudring^{c,d,e}, Bo Brummerstedt Iversen^{c,d}, Yuji Furukawa^{a,b}, and David C. Johnston^{a,b,2}

^aAmes Laboratory, Iowa State University, Ames, IA 50011; ^bDepartment of Physics and Astronomy, Iowa State University, Ames, IA 50011; ^cCenter for Materials Crystallography, Department of Chemistry, Aarhus University, DK-8000 Aarhus C, Denmark; ^diNANO, Aarhus University, DK-8000 Aarhus C, Denmark; and ^eDepartment of Materials and Environmental Chemistry, Stockholm University, 106 91 Stockholm, Sweden

Edited by Zachary Fisk, University of California, Irvine, CA, and approved September 28, 2021 (received for review May 10, 2021)

SrMn₂P₂ and CaMn₂P₂ are insulators that adopt the trigonal CaAl₂Si₂-type structure containing corrugated Mn honeycomb layers. Magnetic susceptibility χ and heat capacity versus temperature T data reveal a weak first-order antiferromagnetic (AFM) transition at the Néel temperature $T_N = 53(1)$ K for SrMn₂P₂ and a strong first-order AFM transition at $T_N = 69.8(3)$ K for CaMn₂P₂. Both compounds exhibit isotropic and nearly T -independent $\chi(T \leq T_N)$, suggesting magnetic structures in which nearest-neighbor moments are aligned at $\approx 120^\circ$ to each other. The ³¹P NMR measurements confirm the strong first-order transition in CaMn₂P₂ but show critical slowing down above T_N for SrMn₂P₂, thus also evidencing second-order character. The ³¹P NMR measurements indicate that the AFM structure of CaMn₂P₂ is commensurate with the lattice whereas that of SrMn₂P₂ is incommensurate. These first-order AFM transitions are unique among the class of (Ca, Sr, Ba)Mn₂(P, As, Sb, Bi)₂ compounds that otherwise exhibit second-order AFM transitions. This result challenges our understanding of the circumstances under which first-order AFM transitions occur.

first-order antiferromagnetic transitions | SrMn₂P₂ | CaMn₂P₂ | trigonal CaAl₂Si₂ structure | incommensurate and commensurate antiferromagnetic structures

The Mn-based 122-type pnictides AMn₂Pn₂ ($A = \text{Ca, Sr, Ba; } Pn = \text{P, As, Sb, Bi}$) have received attention owing to their close stoichiometric 122-type relationship to high- T_c iron pnictides. The undoped Mn pnictides are local-moment antiferromagnetic (AFM) insulators like the high- T_c cuprate parent compounds (1–3). The BaMn₂Pn₂ compounds crystallize in the body-centered tetragonal ThCr₂Si₂ structure as in AFe₂As₂ ($A = \text{Ca, Sr, Ba, Eu}$), whereas the (Ca,Sr)Mn₂Pn₂ compounds crystallize in the trigonal CaAl₂Si₂-type structure (4). Recently, density-functional theory (DFT) calculations for the 122 pnictide family have suggested that the trigonal 122 transition-metal pnictides that have the CaAl₂Si₂ structure might compose a new family of magnetically frustrated materials in which to study the potential superconducting mechanism (5, 6). It had previously been suggested on theoretical grounds that CaMn₂Sb₂ is a fully frustrated classical magnetic system arising from proximity to a tricritical point (7–9).

The electrical resistivity ρ and heat capacity C_p versus temperature T of single-crystal CaMn₂P₂ were reported in ref. 10. The compound is an insulator at $T = 0$ and undergoes a first-order transition of some type at 69.5 K. The Raman spectrum of CaMn₂P₂ at $T = 10$ K showed new peaks compared to the spectrum at 300 K, whereas the authors' single-crystal X-ray diffraction measurements showed no difference in the crystal structure at 293 and 40 K. They suggested that the results of the two types of measurements could be reconciled if a superstructure formed below 69.5 K (10). The authors' magnetic susceptibility $\chi(T)$

measurements below 400 K revealed no evidence for a magnetic transition.

Here we report the detailed properties of trigonal CaMn₂P₂ and SrMn₂P₂ (11) single crystals. We present the results of single-crystal X-ray diffraction (XRD), electrical resistivity ρ in the ab plane (hexagonal unit cell) versus temperature T , isothermal magnetization versus applied magnetic field $M(H)$, magnetic susceptibility $\chi(T)$, heat capacity $C_p(H, T)$, and ³¹P NMR measurements. We find from $C_p(T)$, $\chi(T)$, and NMR that CaMn₂P₂ exhibits a strong first-order AFM transition at $T_N = 69.8(3)$ K whereas SrMn₂P₂ shows a weak first-order transition at $T_N = 53(1)$ K but with critical slowing down on approaching T_N from above as revealed from NMR, a characteristic feature of second-order transitions. Thus, remarkably, the AFM transition in SrMn₂P₂ has characteristics of both first- and second-order transitions. The $\chi(T)$ data also reveal the presence of strong isotropic AFM spin fluctuations in the paramagnetic (PM) state above T_N up to our maximum measurement temperatures of 900 and 350 K for SrMn₂P₂ and CaMn₂P₂, respectively.

Significance

With rare exceptions, an antiferromagnetic (AFM) transition in zero magnetic field is thermodynamically of second order where the thermal-average magnetic moments of the magnetic atoms (ordered moments) vary continuously on cooling through the AFM ordering temperature T_N with no latent heat at the transition. Such materials include the AFM pnictides CaMn₂As₂, SrMn₂As₂, CaMn₂Sb₂, SrMn₂Sb₂, and CaMn₂Bi₂. Here we demonstrate that the closely related SrMn₂P₂ and CaMn₂P₂ insulators instead exhibit first-order AFM transitions at $T_N = 53$ and 70 K, respectively, where the heat capacity exhibits a latent heat at T_N . The mechanism causing these first-order transitions remains to be explained, but its understanding may lead to the development of novel magnetic materials of technological interest.

Author contributions: N.S.S., B.B.I., Y.F., and D.C.J. designed research; N.S.S., S.P., Q.-P.D., L.K., H.-C.L., V.S., A.-V.M., B.B.I., Y.F., and D.C.J. performed research; N.S.S., S.P., Q.-P.D., L.K., H.-C.L., V.S., A.-V.M., B.B.I., Y.F., and D.C.J. analyzed data; and N.S.S., S.P., V.S., A.-V.M., B.B.I., Y.F., and D.C.J. wrote the paper.

The authors declare no competing interest.

This article is a PNAS Direct Submission.

Published under the PNAS license.

¹Present address: Institute for Experimental Physics IV, Ruhr University Bochum, 44801 Bochum, Germany.

²To whom correspondence may be addressed. Email: johnston@ameslab.gov.

This article contains supporting information online at <https://www.pnas.org/lookup/suppl/doi:10.1073/pnas.2108724118/-DCSupplemental>.

Published October 29, 2021.

This behavior likely arises from spin fluctuations associated with the quasi-two-dimensional nature of the Mn spin layers (12) together with possible contributions from magnetic frustration. Our single-crystal XRD data at room temperature and high-resolution synchrotron XRD data at $T = 20$ K for SrMn_2P_2 and CaMn_2P_2 demonstrate conclusively that there is no structure change of either compound on cooling below their respective T_N .

Our studies of SrMn_2P_2 and CaMn_2P_2 thus identify the only known members of the class of materials with general formula $A\text{Mn}_2\text{Pn}_2$ containing Mn^{2+} spins $S = 5/2$ that exhibit first-order AFM transitions, where $A = \text{Ca}, \text{Sr},$ or Ba and the pnictogen $\text{Pn} = \text{P}, \text{As}, \text{Sb},$ or Bi . In particular, only second-order AFM transitions are found in CaMn_2As_2 (13), SrMn_2As_2 (13–15), CaMn_2Sb_2 (8, 9, 16–19), SrMn_2Sb_2 (16, 19), and CaMn_2Bi_2 (20).

Results and Discussion

Crystallography and Chemical Analysis. Scanning electron-microscope (SEM) images of the crystal surfaces indicated single-phase crystals. Energy-dispersive X-ray spectroscopy analyses of the chemical compositions were in agreement with the expected 1:2:2 composition of the compounds and the amount of Sn incorporated into the crystal structure from the Sn

flux is zero to within the experimental error. Single-crystal XRD measurements on CaMn_2P_2 and SrMn_2P_2 confirmed the single-phase nature of the compounds and the CaAl_2Si_2 -type crystal structure of each as shown in *SI Appendix*. The lattice parameters a and c of the trigonal structure (hexagonal unit cell) are in good agreement with previous values (10, 11). The crystal structures of each of CaMn_2P_2 and SrMn_2P_2 at room temperature and 20 K were found to be the same as noted above.

Electrical Resistivity. The $\rho(T)$ data for currents within the basal ab plane of the crystals from 270 to 400 K for SrMn_2P_2 and from 150 to 300 K for CaMn_2P_2 were measured as discussed in *SI Appendix*. The compounds are insulating for $T \rightarrow 0$ K with intrinsic activation energies $\Delta = 0.124(3)$ eV for SrMn_2P_2 and $\Delta = 0.088(1)$ eV for CaMn_2P_2 .

Magnetic Susceptibility. Fig. 1A shows the zero-field-cooled (ZFC) magnetic susceptibility $\chi(T) \equiv M(T)/H$ of SrMn_2P_2 in a magnetic field $H = 0.1$ T applied in the ab plane (χ_{ab}) and along the c axis (χ_c). These data exhibit an AFM transition at $T_N = 53(1)$ K, clearly seen from the peak in the expanded plot of $d(\chi_c T)/dT$ versus T in Fig. 1B according to the Fisher relation (21). The $\chi(T)$ below T_N is almost isotropic and the magnetic phase transition is sharper in $\chi_c(T)$.

Fig. 2 shows $\chi(T)$ of SrMn_2P_2 from 1.8 to 900 K measured in $H = 3$ T. Similar $\chi(T)$ data were obtained previously for a polycrystalline sample of SrMn_2P_2 (14, 22). Unlike most local-moment antiferromagnets for which $\chi(T)$ decreases above T_N according to the Curie-Weiss law, the $\chi(T)$ above T_N in SrMn_2P_2 increases with T , exhibits a broad maximum at about 400 K, and then slowly decreases. Therefore, the present data suggest that strong dynamic AFM correlations occur up to at least 900 K, similar to corresponding data for the isostructural compounds $(\text{Sr,Ca})\text{Mn}_2(\text{As,Sb})_2$ (13, 19). Within a local-moment picture, these features at $T > T_N$ are consistent with SrMn_2P_2 being a quasi-two-dimensional antiferromagnet. In *SI Appendix* an estimate of the exchange interactions J between the Mn spins-5/2 in SrMn_2P_2 is obtained from the $\chi_{ab}(T)$ data in Fig. 2. If only nearest-neighbor AFM interactions are assumed to occur between a Mn spin and its three Mn neighbors within the two-dimensional puckered honeycomb lattice, we obtain $J \sim 34$ meV or $J/k_B \sim 400$ K in temperature units. This result suggests the presence of strong AFM fluctuations arising from the

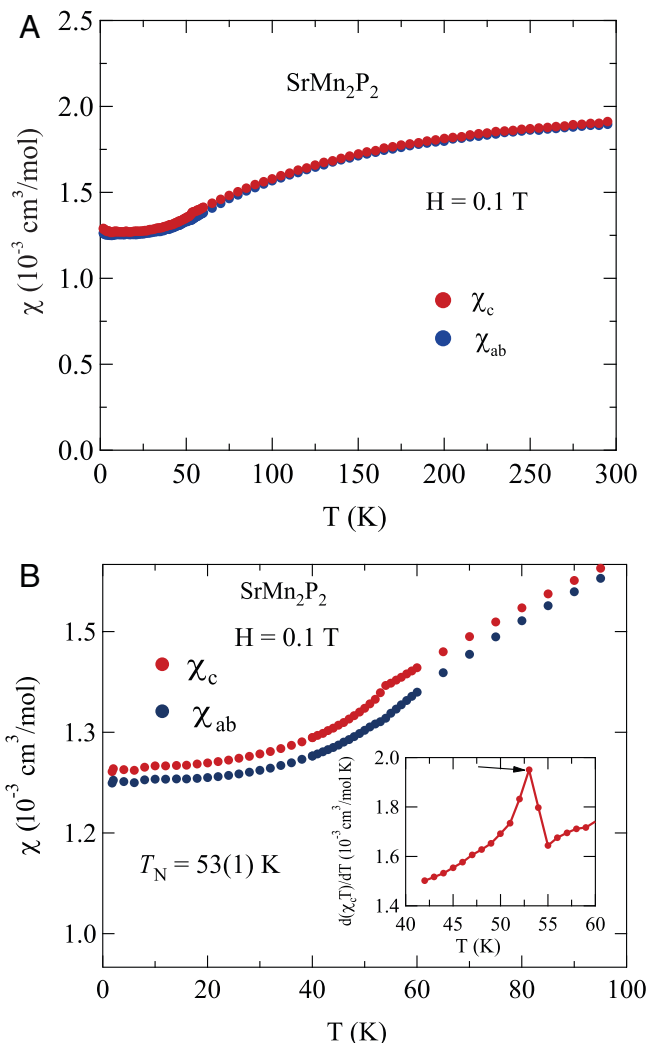


Fig. 1. (A) Temperature-dependent zero-field-cooled magnetic susceptibility $\chi(T)$ of SrMn_2P_2 in a magnetic field $H = 0.1$ T applied in the ab plane (χ_{ab}) and along the c axis (χ_c). (B) Expanded plot of $\chi(T)$ between 1.8 and 100 K to highlight the transition. (Inset) Derivative $d[\chi_c(T)T]/dT$ versus T for $H \parallel c$, yielding $T_N = 53(1)$ K as indicated by the arrow.

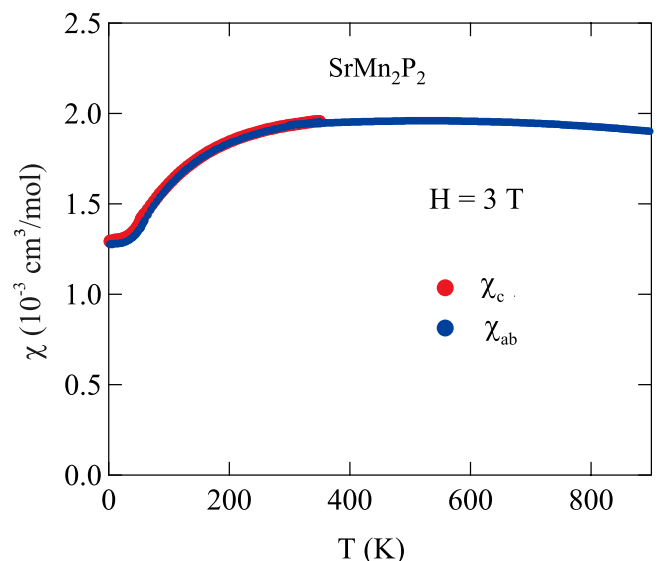


Fig. 2. Zero-field-cooled magnetic susceptibility χ_{ab} and χ_c versus T for $1.8 \text{ K} \leq T \leq 900 \text{ K}$ measured in $H = 3$ T.

quasi-two-dimensional nature of the honeycomb lattice (23) and/or of frustrating magnetic interactions between the Mn spins.

$M(H)$ isotherms for single crystals of SrMn_2P_2 and CaMn_2P_2 with $H \parallel ab$ and $H \parallel c$ are shown in *SI Appendix*. The data for M_{ab} and M_c are proportional to H at all temperatures, indicating the absence of significant ferromagnetic or saturable paramagnetic impurities. The nearly isotropic $M(H, T < T_N)$ data for both field directions are consistent with the nearly isotropic behavior of $\chi(T \leq T_N)$ in Figs. 1 and 2, as well as Fig. 3*B* below.

The ZFC magnetic susceptibilities $\chi \equiv M/H$ versus T measured in $H = 0.1$ T and $H = 3$ T applied in the ab plane ($H \parallel ab$, χ_{ab}) and along the c axis ($H \parallel c$, χ_c) for a single crystal of CaMn_2P_2 are shown in Fig. 3*A* and *B*, respectively. At first glance, there is no clear feature of any magnetic phase transition up to 350 K. However, an expanded plot of the $\chi_c(T)$ data in Fig. 4, *Inset* shows a first-order AFM transition at ≈ 69 K. The temperature derivative of $\chi(T)$ versus T is plotted for both χ_{ab}

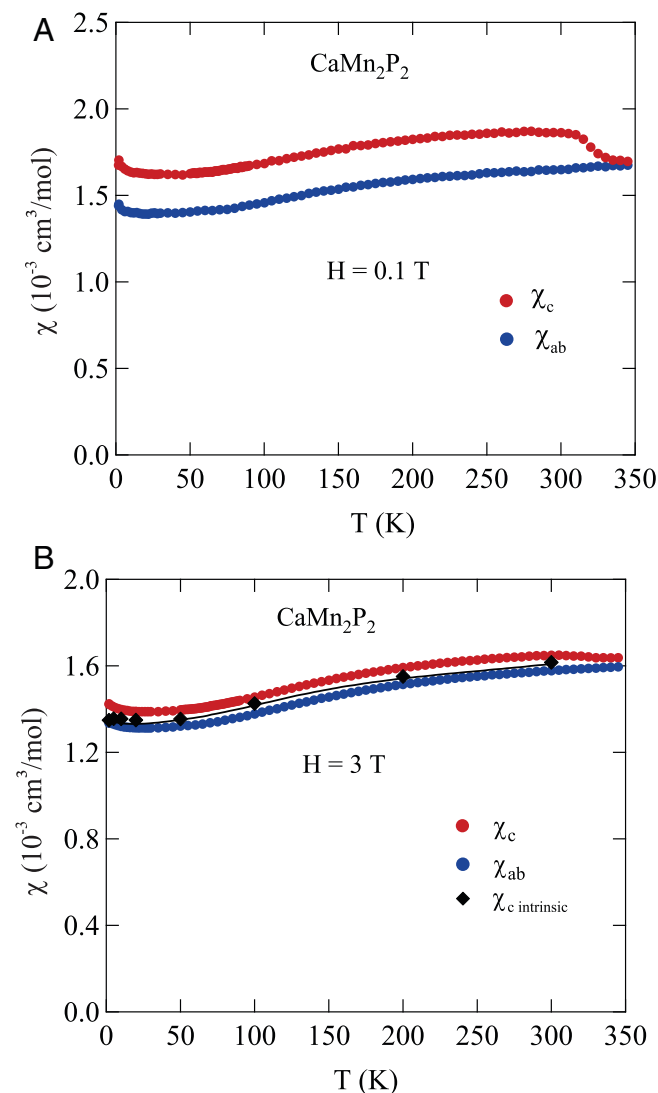


Fig. 3. Temperature-dependent zero-field-cooled magnetic susceptibility $\chi(T)$ of CaMn_2P_2 in magnetic fields (A) $H = 0.1$ T and (B) $H = 3$ T applied in the ab plane (χ_{ab}) and along the c axis (χ_c). In B, the intrinsic $\chi_c(T)$ data also obtained from the high-field slope of $M(H)$ isotherms in *SI Appendix* are also included, denoted as $\chi_{c \text{ intrinsic}}$. In A, the increase in the $\chi_c(T)$ data on cooling below 350 K is inferred to arise from a very small amount of ferromagnetic MnP impurity, whereas in B the impurity magnetization is not as evident in the 3-T field.

and χ_c in Fig. 4, where the first-order nature of the magnetic transition in $\chi_c(T)$ is more clearly evident and yields the more precise $T_N = 69.8(3)$ K.

Like SrMn_2P_2 , CaMn_2P_2 is a low-dimensional antiferromagnet as seen by the very broad apparent maximum in $\chi(T)$ above T_N in Fig. 3*B*. Indeed, the Curie-Weiss temperature region of χ is not reached up to 350 K, indicating that strong AFM correlations survive to significantly higher temperatures than plotted. Previous studies of Mn pnictides suggested that for the d^5 electronic configuration of Mn^{2+} ($S = 5/2$) in trigonal Mn pnictides, the nearest-neighbor interactions are very strong and these compounds tended to have AFM correlations or develop long-range AFM order due to the competition among different exchange interactions between the Mn sites (2, 5, 13, 19).

In addition, a small upturn in $\chi_c(T)$ is seen in Fig. 3*A* below about 300 K. This is likely due to ferromagnetic (FM) MnP impurities with Curie temperature $T_c = 291.5$ K (24) that are present on the crystal surface and/or as an inclusion in the crystal, similar to BaMn_2As_2 (2) and SrMn_2As_2 (13) crystals with MnAs impurities. From a comparison of Fig. 3*A* and *B*, this FM MnP impurity is most clearly seen in the $\chi_c(T)$ data with $H = 0.1$ T. In addition, there is a small upturn in $\chi(T)$ data below ≈ 40 K, which is likely due to the contribution of paramagnetic impurities.

From the nearly isotropic and T -independent $\chi(T)$ of CaMn_2P_2 and SrMn_2P_2 below T_N in Figs. 1*B* and 3*B*, respectively, we suggest that the AFM structures in both compounds are, or are similar to, a $\approx 120^\circ$ c -axis helix or ab -plane cycloid (25, 26).

Heat Capacity. Fig. 5*A* and *B* shows zero-field $C_p(T)$ data for SrMn_2P_2 and CaMn_2P_2 , respectively. The sharp peaks in $C_p(T)$ at 53 K in SrMn_2P_2 and at 69.8 K in CaMn_2P_2 are at the respective Néel temperatures of the two compounds found from the above $\chi(T)$ data. The $C_p(T)$ value obtained at 300 K is smaller than the classical Dulong-Petit limit of $3nR \sim 124$ J/mol-K for both compounds and similar to that reported in ref. 10 for CaMn_2P_2 . Figs. 2 and 3 demonstrate that strong dynamic short-range AFM correlations persist up to high temperatures, as was previously found for the isostructural compounds CaMn_2As_2 and SrMn_2As_2 (13). Thus, extraction of the T -dependent lattice contribution to the heat capacity below 300 K that could then

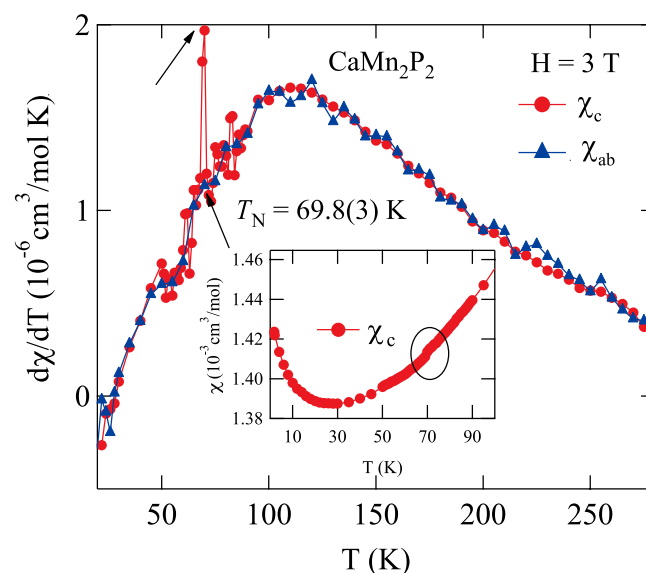


Fig. 4. Temperature derivative of the magnetic susceptibility $d\chi(T)/dT$ of CaMn_2P_2 in Fig. 3*B*. (*Inset*) Expanded plot of $\chi_c(T)$ to highlight the first-order AFM transition at $T_N = 69.8(3)$ K.

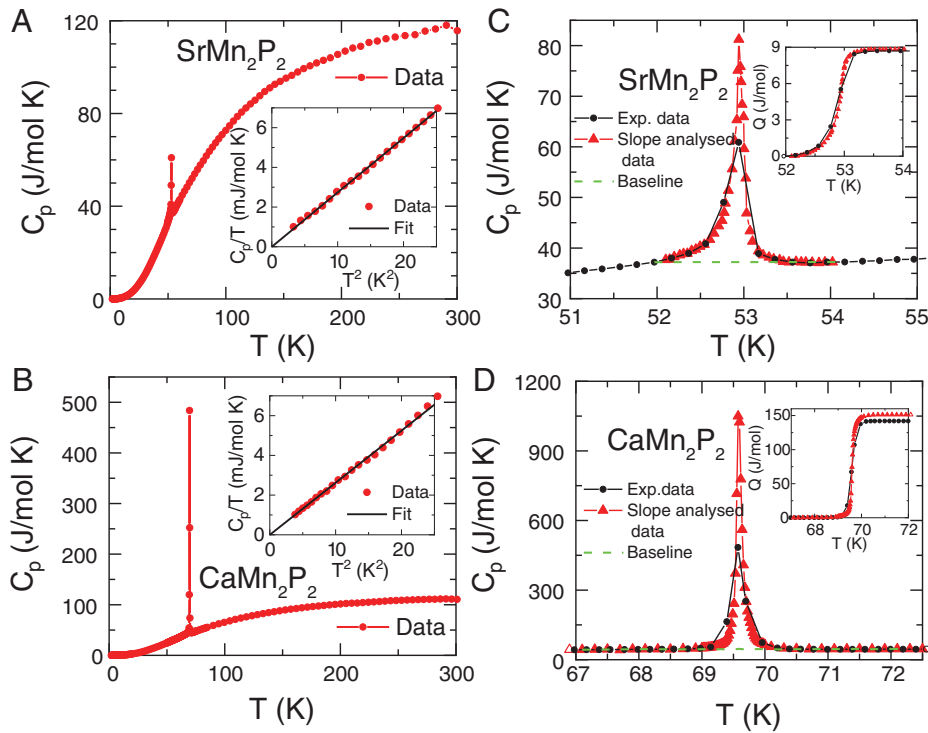


Fig. 5. Heat capacity C_p versus temperature T for (A) SrMn_2P_2 and (B) CaMn_2P_2 single crystals. (A and B, Insets) $C_p(T)/T$ versus T^2 for $T \leq 5$ K, where the straight lines through the respective data are fits by Eq. 1. A comparison of the conventionally measured $C_p(T)$ and single-pulse slope-analyzed $C_p(T)$ (using a heating curve) is shown for (C) SrMn_2P_2 and (D) CaMn_2P_2 crystals. (C and D, Insets) The latent heat associated with the first-order magnetic transition (FOMT). The $C_p(T)$ values at the FOMT are estimated by subtracting the polynomial-fitted baseline data (dashed green line) from the total $C_p(T)$ data in that temperature region shown in C and D.

reveal the T dependence of the magnetic contribution is not possible with the information available.

Fig. 5 A and B, Insets show $C_p(T)/T$ versus T^2 between 1.8 and 5 K. The data were fitted by

$$C_p/T = \beta T^2 \quad [1]$$

appropriate to insulators, where β reflects the low- T lattice contribution that we assume does not contain a three-dimensional AFM spin-wave contribution. From the fits of Eq. 1 to the data in Fig. 5 A and B, Insets, we obtain $\beta = 0.273(1)$ mJ/(mol K⁴) for SrMn_2P_2 and $0.262(1)$ mJ/(mol K⁴) for CaMn_2P_2 . The Debye temperature θ_D is given by

$$\theta_D = \left(\frac{12\pi^4 R n}{5\beta} \right)^{1/3}, \quad [2]$$

where R is the molar gas constant and n is the number of atoms per formula unit [$n = 5$ for (Sr or Ca) Mn_2P_2]. Using the above β values we obtain $\theta_D = 329(3)$ and $314(1)$ K for SrMn_2P_2 and CaMn_2P_2 , respectively.

As seen in Fig. 5 A and B, for both SrMn_2P_2 and CaMn_2P_2 a very narrow heat-capacity peak occurs at T_N , and the heights of these peaks indicate the occurrence of weak and strong first-order transitions, respectively. Near T_N , the experimental $C_p(T)$ data were corrected using the single-pulse slope-analysis method with heating curves as described in SI Appendix and shown in Fig. 5 C and D. The latent heat Q associated with the first-order magnetic transition for each compound was calculated by first subtracting the respective $C_p(T)$ backgrounds using a polynomial fit and then measuring the area under the resultant peak as shown in Fig. 5 C and D. For SrMn_2P_2 we obtained $Q \approx 8.7$ J/mol at $T_N \approx 53$ K, whereas for CaMn_2P_2 we obtained $Q \approx 152$ J/mol at $T_N = 69.5$ K. The sharp C_p peak value for CaMn_2P_2 obtained

from the slope-analyzed measurements in Fig. 5B is significantly larger than obtained previously (10). As shown in SI Appendix, an applied field $H = 9$ T has negligible influence on $C_p(T \approx T_N)$ for both SrMn_2P_2 and CaMn_2P_2 , respectively, as also found for CaMn_2P_2 in ref. 10.

NMR. Fig. 6A shows the typical T dependence of ^{31}P NMR spectra for the $H \parallel ab$ plane in SrMn_2P_2 . Above T_N , a single line expected for the nuclear spin $I = 1/2$ NMR spectrum is observed. The details of the observed NMR spectra in the paramagnetic state and their analysis are given in SI Appendix. When T is lowered close to $T_N \approx 53$ K, as shown in Fig. 6A, the single sharp NMR line (denoted by P_{HT}) suddenly broadens due to the internal field (H_{int}) at the P site produced by the Mn^{2+} ordered moments in the AFM state. The observed spectra become nearly independent of T below 40 K as shown in Fig. 6C, where the two peak positions denoted by P1 (H_{P1}) and P2 (H_{P2}) in Fig. 6A are plotted versus T .

The internal field H_{int} , which is proportional to the Mn^{2+} sublattice magnetization, was determined as half of the separation between P1 and P2. The temperature dependences of H_{int} are shown in Fig. 6D from which we estimated the critical exponent of the order parameter (sublattice magnetization). H_{int} was fitted by the power law $H_{\text{int}} = H_{\text{int},0}(1 - T/T_N)^\beta$ with $T_N = 53.0$ K. The solid line in Fig. 6D shows the curve with $H_{\text{int},0} = 0.175$ T and $\beta = 0.13$. Here the value of β is much smaller than expected for any three-dimensional magnetic material with a second-order phase transition such as $\beta = 0.33$ to 0.367 for three-dimensional (3D) Heisenberg, 0.31 to 0.345 for 3D XY, and 0.31 to 0.326 for 3D Ising models (27), but close to 0.125 for the two-dimensional (2D) Ising model (27). These results suggest a second-order phase transition. In addition, we followed the reduction in H_{int} near T_N and also detected a critical slowing-down behavior in the T dependence of the ^{31}P

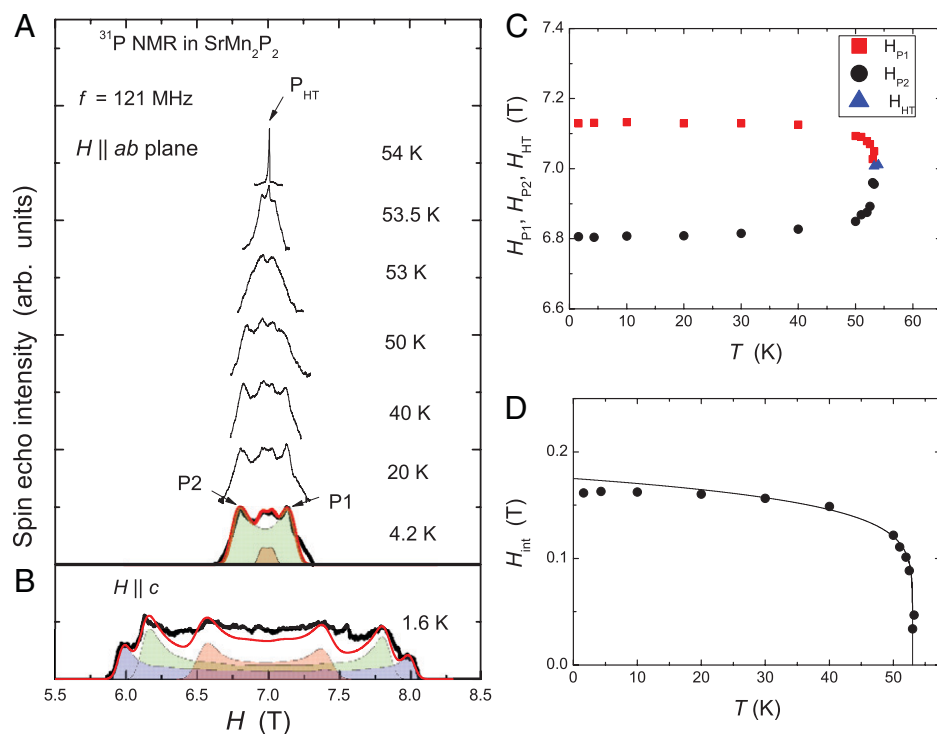


Fig. 6. (A) Field-swept ^{31}P -NMR spectra at a resonance frequency of $f = 121$ MHz for H parallel to the ab plane at various temperatures in SrMn_2P_2 below T_N . The black curves are the observed spectra. The green and light-red areas are calculated spectra with an incommensurate helical AFM state with different internal fields of $H_{\text{int}} = 2.0$ and 0.5 kOe, respectively. The red curve is the sum of the two calculated spectra. (B) Field-swept ^{31}P -NMR spectrum at 1.6 K for $H \parallel c$. The black curves are the observed spectra and the other colored areas and line are the same with different internal fields (main text). (C) Temperature dependence of the peak positions for P_{HT} , P_1 , and P_2 defined in A. (D) Temperature dependence of $H_{\text{int}} = (H_{P_1} - H_{P_2})/2$. The solid line is the calculated $H_{\text{int}} = H_{\text{int},0}(1 - T/T_N)^\beta$ with $H_{\text{int},0} = 0.175$ T, $\beta = 0.13$, and $T_N = 53.0$ K.

spin-lattice relaxation rate $1/T_1$ around T_N (shown below). Therefore, the magnetic phase transition for SrMn_2P_2 is considered to be characterized as a second-order phase transition. However, the above $C_p(T)$ data suggest a weak first-order transition, so the transition at T_N has characteristics of both orders of the transition.

The broad NMR spectra observed below T_N indicate a distribution of internal fields H_{int} , which is reminiscent of a two-horn structure expected for an incommensurate helical structure, as has been observed in EuCo_2P_2 (28) and EuCo_2As_2 (29). In fact, the observed spectrum is reasonably reproduced by that calculated for an incommensurate helical AFM state shown by the green area in Fig. 6A, assuming an internal field along the ab plane $H_{\text{int},ab} = 2.0$ kOe, although we note that one needs to introduce another P site with a smaller $H_{\text{int},ab} = 0.5$ kOe (shown by the light red area). The red curve is the sum of two calculated spectra that reproduces the observed spectrum. We note a small deviation between the calculated and the observed spectra, especially at the tail of the spectrum. This suggests another P site with a slightly different internal field as will be seen in the NMR spectrum for $H \parallel c$ described below. Although the multiple P sites may suggest a structural phase transition, the previous neutron-diffraction (14) and our single-crystal X-ray diffraction measurements (SI Appendix) revealed no change in the crystal structure below T_N of SrMn_2P_2 . The origin of the multiple P sites is not clear at present; however, it is most likely due to a complicated magnetic structure in SrMn_2P_2 (ref. 14 and SI Appendix).

A similar, but much broader, two-horn-like spectrum was observed for $H \parallel c$ in the AFM state as shown in Fig. 6B. Here we measured the spectrum only at 1.6 K and not at higher T due to poor signal intensity. The observed spectrum was also reasonably reproduced by a calculated spectrum for an incommensurate

AFM state where we assumed three different P sites with different internal fields along the c axis: $H_{\text{int},c} = 10$ kOe (blue area), $H_{\text{int},c} = 8.5$ kOe (green area), and $H_{\text{int},c} = 4.5$ kOe (light red area). Although the observed spectrum was not perfectly reproduced by the calculated spectrum, we consider that the analysis captures the essential point, evidencing the incommensurate AFM state in SrMn_2P_2 .

Our NMR results are consistent with previous $\chi(T)$ data for a polycrystalline SrMn_2P_2 sample and associated powder neutron-diffraction data (14) that suggested the presence of a complex low-dimensional (30) incommensurate AFM structure of high-spin Mn^{2+} below $T_N = 52(2)$ K with significant short-range AFM order well above T_N .

Similar ^{31}P -NMR measurements were performed on CaMn_2P_2 . As in the case of SrMn_2P_2 , a single NMR line was observed in the paramagnetic state (for details, see SI Appendix). Although the ^{31}P NMR spectra in the PM state are similar to those observed in SrMn_2P_2 , surprisingly, the ^{31}P NMR spectra in the AFM state below T_N are quite different from the case of SrMn_2P_2 . As shown in Fig. 7A for $H \parallel c$, the single NMR line (denoted by P_{HT}) observed in the PM state suddenly splits below T_N into mainly three lines at higher and lower magnetic-field positions with a double-peak structure (denoted by P_1 , P_2 , P_4 , and P_5) and around a nearly zero-shift position (P_3). The detailed changes in the NMR spectrum around the zero-shift position are shown in Fig. 7C. Note here we measured the spectrum with increasing T . No P_{HT} signal from the PM state could be observed and only the signal (P_3) from the AFM state was detected at 68 K. Then, P_{HT} starts to appear at 69.8 K and the P_3 signal disappears completely at 70.2 K. The coexistence of the two signals from the AFM and PM states can be seen in a quite narrow temperature range from 69.8 to 70 K, indicating a very small hysteresis in the first-order transition.

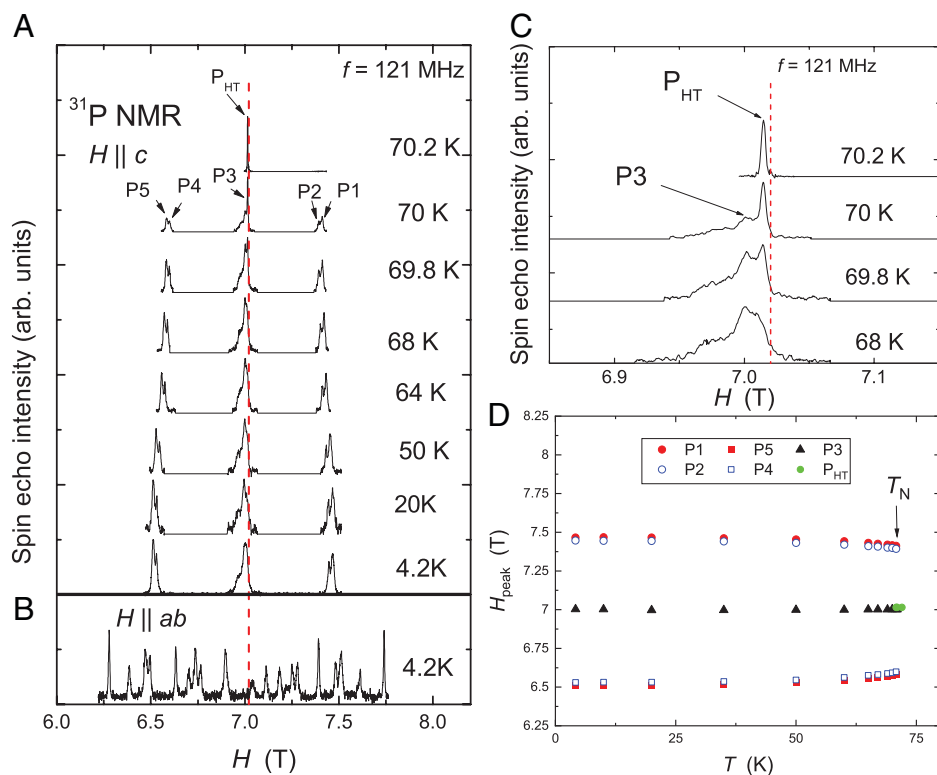


Fig. 7. (A) Field-swept ^{31}P -NMR spectra at a resonance frequency $f = 121$ MHz for $H \parallel c$ in CaMn_2P_2 at various T below T_N . The vertical dashed line at $H = 7.0204$ T represents the zero-shift position ($K = 0$). (B) Field-swept ^{31}P -NMR spectrum at 4.2 K for $H \parallel ab$. (C) Expanded ^{31}P NMR spectra near the zero-shift position for temperatures near T_N . (D) Temperature dependence of the peak positions for P_{HT} and P1 to P5 defined in A.

The distinct splittings of the NMR line below T_N clearly indicate that the AFM state is commensurate in CaMn_2P_2 , which is in strong contrast to the case of the incommensurate AFM state in SrMn_2P_2 . Similar distinct splittings of NMR lines were also observed for $H \parallel ab$, where a more complicated spectrum with at least 20 peaks was detected (Fig. 7B). Although the spectrum is complicated and suggests a complex magnetic structure, it is clear that the commensurate nature holds not only along the c axis but also in the ab plane. The multiple peaks in the NMR spectra indicate the presence of several P sites with different internal fields in the AFM state of CaMn_2P_2 , as in the case of SrMn_2P_2 . Although a possible superlattice crystal structure below T_N in CaMn_2P_2 has been suggested (10), our high-resolution single-crystal synchrotron X-ray diffraction measurements at 20 K exclude the possibility of superlattice formation below T_N (SI Appendix). Therefore, the origin of the multiple P sites is most likely due to a complex magnetic structure in CaMn_2P_2 as is the case of SrMn_2P_2 .

Fig. 7D shows the T dependence of the peak positions for $H \parallel c$. Clear jumps in the positions due to a finite internal field at T_N can be seen. These results clearly show that the AFM phase transition in CaMn_2P_2 is of first order, consistent with the results of the $C_p(T)$ measurements.

The different nature of the AFM transitions for SrMn_2P_2 and CaMn_2P_2 can also be seen in the T dependence of the ^{31}P spin-lattice relaxation rate $1/T_1$. Fig. 8 shows the T dependence of $1/T_1 T$ for SrMn_2P_2 and CaMn_2P_2 for H parallel to the c axis and to the ab plane.

For SrMn_2P_2 , with decreasing T , $1/T_1 T$ for both field directions gradually increases and is strongly enhanced below ~ 60 K. For $H \parallel ab$, $1/T_1 T$ starts to decrease just below $T_N = 53$ K, exhibiting a clear peak in $1/T_1 T$ that is usually explained by critical slowing down of spin fluctuations as expected for a second-order phase transition.

In contrast, $1/T_1 T$ for both magnetic-field directions in CaMn_2P_2 does not exhibit a clear enhancement close at T_N , indicating no critical slowing down of the Mn spins as expected for a first-order phase transition. In addition, $1/T_1 T$

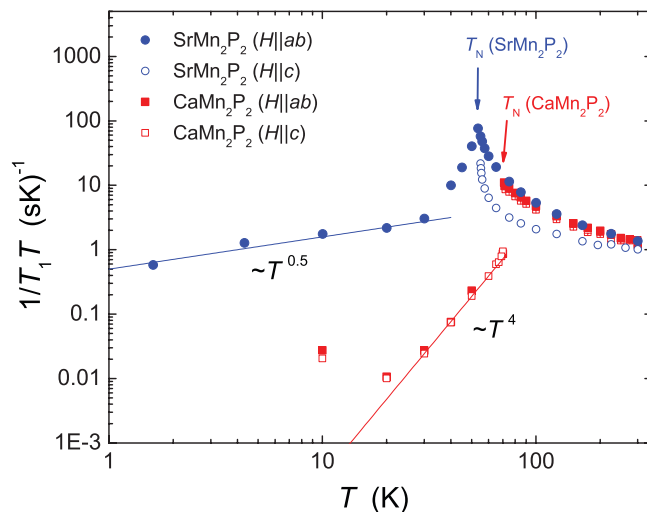


Fig. 8. Temperature dependence of $1/T_1 T$ for SrMn_2P_2 and CaMn_2P_2 for both magnetic-field directions $H \parallel c$ axis and $H \parallel ab$ plane. The blue solid and open circles are the results for SrMn_2P_2 with $H \parallel ab$ and $H \parallel c$, respectively. In the AFM state of SrMn_2P_2 , $1/T_1 T$ was measured at nearly zero-shift positions for $H \parallel ab$. The red solid and open squares are the results for CaMn_2P_2 with $H \parallel ab$ and $H \parallel c$, respectively. In the AFM state of CaMn_2P_2 , $1/T_1 T$ was measured at the P3 position for $H \parallel c$ and at the lowest-field peak position for $H \parallel ab$. The blue and red straight lines show the power-law dependencies $1/T_1 T \propto T^{0.5}$ and T^4 for SrMn_2P_2 and CaMn_2P_2 , respectively.

shows a discontinuous decrease just below T_N , which again confirms the first-order nature of the AFM phase transition in CaMn_2P_2 .

Fig. 8 shows that below T_N , $1/T_1 T$ shows $T^{0.5}$ and T^4 power-law behaviors for SrMn_2P_2 and CaMn_2P_2 , respectively. In the AFM state, $1/T_1 T$ is mainly driven by scattering of magnons, leading to T^2 and T^4 power-law T dependencies due to a two- or three-magnon Raman process, respectively (31). The weak T dependence $1/T_1 T \propto T^{0.5}$ below 40 K for SrMn_2P_2 cannot be explained by magnon scattering and suggests the presence of other magnetic fluctuations in the magnetically ordered state. On the other hand, the T^4 power-law behavior observed in CaMn_2P_2 is consistent with T^4 expected for the three-magnon relaxation process in AFM materials where the deviation from the power-law behavior for $T \lesssim 20$ K could be due to relaxation associated with impurities.

Finally, we discuss the magnetic fluctuations in the PM state of SrMn_2P_2 and CaMn_2P_2 . In general, $1/T_1 T$ can be expressed in terms of the imaginary part of the dynamic susceptibility $\chi''(\vec{q}, \omega_0)$ per mole of electronic spins as (32)

$$\frac{1}{T_1 T} = \frac{2\gamma_N^2 k_B}{N_A^2} \sum_{\vec{q}} |A(\vec{q})|^2 \frac{\chi''(\vec{q}, \omega_0)}{\omega_0}, \quad [3]$$

where γ_N is the nuclear gyromagnetic ratio, the sum is over the wave vectors \vec{q} within the first Brillouin zone, $A(\vec{q})$ is the form factor of the hyperfine interactions, and $\chi''(\vec{q}, \omega_0)$ is the imaginary part of the dynamic susceptibility at the Larmor frequency ω_0 . On the other hand, the uniform χ corresponds to the real component $\chi'(\vec{q}, \omega_0)$ with $q = 0$ and $\omega_0 = 0$. Therefore, the increase of $1/T_1 T$ and the slight decrease of χ with decreasing T imply that $\sum_{\vec{q}} |A(\vec{q})|^2 \chi''(\vec{q}, \omega_0)$ increases, evidencing a growth of spin correlations with $q \neq 0$ for both systems. Thus, we conclude that AFM spin fluctuations exist in the PM states in SrMn_2P_2 and CaMn_2P_2 . We also point out that from the smooth extrapolation of the T dependence of $1/T_1 T$, the AFM fluctuations seem to persist up to temperature much higher than 300 K, consistent with the $\chi(T)$ results discussed above and the analysis of $\chi(T \gg T_N)$ of SrMn_2P_2 in *SI Appendix*.

Discussion. Our $\chi(H, T)$ and $C_p(T)$ measurements reveal first-order AFM transitions at $T_N = 53(1)$ and $69.8(3)$ K for SrMn_2P_2 and CaMn_2P_2 , respectively. First-order AFM transitions in $H = 0$ are rare. Examples include the cubic pyrite-structure insulator MnS_2 containing Mn^{2+} cations with high-spin $S = 5/2$ and $(\text{S}_2)^{2-}$ species with $T_N = 47.7$ K (33, 34), insulating UO_2 with $T_N = 30.8$ K (35), and MnO (36, 37) with $T_N \approx 120$ K. In a series of papers, it was found that symmetry considerations and renormalization-group theory could determine whether or not a given antiferromagnet would exhibit a first-order transition at its Néel temperature (38–41). The theory correctly predicted the occurrence of first-order transitions in the above materials UO_2 and MnO at their respective Néel temperatures. It would be interesting to see whether the same theory would predict the observed first-order AFM transitions in CaMn_2P_2 and SrMn_2P_2 . To utilize this theory, the magnetic structures of SrMn_2P_2 and CaMn_2P_2 below their respective T_N need to be known, where we have ruled out crystal-structure changes below the respective T_N . Experiments to determine the respective magnetic structures are planned. We remark that a structural transition at

T_N was invoked to explain the first-order AFM transition in GeNCr_3 (42).

However, the physical origin(s) of the weak and strong first-order transitions in SrMn_2P_2 and CaMn_2P_2 , respectively, remain to be identified but may originate from the quasi-two-dimensionality of the Mn layers potentially assisted by magnetic frustration. Additional questions to be addressed include the following: Why does SrMn_2P_2 show critical slowing down on approaching T_N from above as revealed from the NMR measurements, which is a characteristic of a second-order transition? A related question is, Why do other similar Mn compounds AMn_2Pn_2 ($A = \text{Ca, Sr, or Ba}$; $\text{Pn} = \text{As, Sb, or Bi}$) discussed in the Introduction not show first-order AFM transitions instead of the observed second-order ones? The answers to these questions may lead to the synthesis and control of magnetic materials with potential technological applications.

Materials and Methods

Single crystals of SrMn_2P_2 and CaMn_2P_2 were grown in Sn flux (10) as described in *SI Appendix*. Shiny platelike hexagon-shaped single crystals of SrMn_2P_2 and CaMn_2P_2 were obtained. Chemical analyses of the single crystals were performed using a JEOL SEM equipped with an energy-dispersive X-ray spectroscopy detector. Single-crystal X-ray structural analyses of SrMn_2P_2 and CaMn_2P_2 were performed at room temperature as detailed in *SI Appendix*. The single-crystal X-ray structural analysis at 20 K was carried out at the SPring8 synchrotron in Japan, as described in *SI Appendix*. Magnetic susceptibility $\chi = M(T)/H$ at fixed applied magnetic field H over the T range $1.8 \leq T \leq 350$ K and $M(H)$ isotherm measurements for $H \leq 5.5$ T were carried out using a Quantum Design, Inc., Magnetic Properties Measurement System. The $M(T)$ for $300 \leq T \leq 900$ K was measured using the vibrating sample magnetometer option of a Quantum Design, Inc., Physical Properties Measurement System (PPMS). Four-probe direct-current $\rho(T)$ and $C_p(T)$ measurements were carried out using the PPMS, where electrical contacts to a crystal for the $\rho(T)$ measurements were made using annealed 0.05-mm-diameter Pt wires attached to the crystals with silver epoxy. The $C_p(T)$ measurements were carried out using the standard relaxation method implemented in the PPMS. However, to measure the latent heat at T_N a different technique was used as described in *SI Appendix*. NMR measurements of ^{31}P nuclei with nuclear spin $I = 1/2$ and gyromagnetic ratio $\gamma_N/2\pi = 17.237$ MHz/T were conducted using a laboratory-built phase-coherent spin-echo pulse spectrometer as described further in *SI Appendix*.

SI Appendix. *SI Appendix* includes details of the crystal growth and chemical analyses, single-crystal structural analyses, electrical resistivity measurements, an estimate of the Heisenberg exchange interaction between nearest-neighbor Mn spins in SrMn_2P_2 , high-temperature magnetic susceptibility data for SrMn_2P_2 , magnetization versus magnetic-field isotherms, measurements of the latent heat in the heat capacity measurements, and ^{31}P NMR measurements.

Data Availability. All study data are included in this article and/or *SI Appendix*.

ACKNOWLEDGMENTS. S.P. is grateful to Dr. Francois Guillou, Inner Mongolia Normal University and Tom Hogan, Quantum Design Applications for helpful communications regarding heat capacity measurements. The research of L.K. and B.B.I. was supported by the Villum Foundation. The research at Ames Laboratory was supported by the US Department of Energy, Office of Basic Energy Sciences, Division of Materials Sciences and Engineering. Ames Laboratory is operated for the US Department of Energy by Iowa State University under Contract DE-AC02-07CH11358. The single-crystal synchrotron X-ray diffraction experiments at temperature 20 K were performed at beamline BL02B1 at SPring8 in Japan with the approval of the Japan Synchrotron Radiation Research Institute. We thank Eiji Nishibori and Seiya Takahashi for assistance with the data collection.

1. J. An, A. S. Sefat, D. J. Singh, M. H. Du, Electronic structure and magnetism in BaMn_2As_2 and BaMn_2Sb_2 . *Phys. Rev. B Condens. Matter Mater. Phys.* **79**, 075120 (2009).
2. Y. Singh, A. Ellern, D. C. Johnston, Magnetic, transport, and thermal properties of single crystals of the layered arsenide BaMn_2As_2 . *Phys. Rev. B Condens. Matter Mater. Phys.* **79**, 094519 (2009).
3. D. C. Johnston et al., Magnetic exchange interactions in BaMn_2As_2 : A case study of the J_1 - J_2 - J_c Heisenberg model. *Phys. Rev. B Condens. Matter Mater. Phys.* **84**, 094445 (2011).

4. E. Brechtel, G. Cordier, H. Schäfer, Presentation and crystal structure of BaMn_2Sb_2 , BaZn_2Sb_2 and BaCd_2Sb_2 . *Mag. für Nature Res. B* **34**, 921–925 (1979).
5. J. Zeng, S. Qin, C. Le, J. Hu, Magnetism and superconductivity in the layered hexagonal transition metal pnictides. *Phys. Rev. B* **96**, 174506 (2017).
6. J. B. Fouet, P. Sindzingre, C. Lhuillier, An investigation of the quantum J_1 - J_2 - J_3 model on the honeycomb lattice. *Eur. Phys. J. B* **20**, 241–254 (2001).
7. I. I. Mazin, CaMn_2Sb_2 : A fully frustrated classical magnetic system. *arXiv:1309.3744* [Preprint] (2013). <https://arxiv.org/abs/1309.3744> (Accessed 22 October 2021).

8. J. W. Simonson *et al.*, Magnetic and structural phase diagram of CaMn_2Sb_2 . *Phys. Rev. B Condens. Matter Mater. Phys.* **86**, 184430 (2012).
9. D. E. McNally *et al.*, CaMn_2Sb_2 : Spin waves on a frustrated antiferromagnetic honeycomb lattice. *Phys. Rev. B Condens. Matter Mater. Phys.* **91**, 180407 (2015).
10. Y. J. Li *et al.*, First-order transition in trigonal structure CaMn_2P_2 . *Europhys. Lett.* **132**, 46001 (2020).
11. A. Mewis, AB_2X_2 -compounds with the CaAl_2Si_2 structure, v[1] the crystal structure of CaMn_2P_2 , CaMn_2As_2 , SrMn_2P_2 and SrMn_2As_2 . *Mag. für Nat. Res. B* **33**, 606–609 (1978).
12. M. E. Lines, Magnetism in two dimensions. *J. Appl. Phys.* **40**, 1352–1358 (1969).
13. N. S. Sangeetha, A. Pandey, Z. A. Benson, D. C. Johnston, Strong magnetic correlations to 900 K in single crystals of the trigonal antiferromagnetic insulators SrMn_2As_2 and CaMn_2As_2 . *Phys. Rev. B* **94**, 094417 (2016).
14. S. L. Brock, J. E. Greedan, S. M. Kauzlarich, Resistivity and magnetism of AMn_2P_2 (A = Sr, Ba): The effect of structure type on physical properties. *J. Solid State Chem.* **113**, 303–311 (1994).
15. P. Das *et al.*, Collinear antiferromagnetism in trigonal SrMn_2As_2 revealed by single-crystal neutron diffraction. *J. Phys. Condens. Matter* **29**, 035802 (2016).
16. S. Bobev *et al.*, Unusual Mn-Mn spin coupling in the polar intermetallic compounds CaMn_2Sb_2 and SrMn_2Sb_2 . *Inorg. Chem.* **45**, 4047–4054 (2006).
17. W. Ratcliff II *et al.*, The magnetic ground state of CaMn_2Sb_2 . *J. Magn. Magn. Mater.* **321**, 2612–2616 (2009).
18. C. A. Bridges *et al.*, Magnetic order in CaMn_2Sb_2 studied via powder neutron diffraction. *J. Magn. Magn. Mater.* **321**, 3653–3657 (2009).
19. N. S. Sangeetha, V. Smetana, A. V. Mudring, D. C. Johnston, Antiferromagnetism in semiconducting SrMn_2Sb_2 and BaMn_2Sb_2 single crystals. *Phys. Rev. B* **97**, 014402 (2018).
20. Q. D. Gibson *et al.*, Magnetic and electronic properties of CaMn_2Bi_2 : A possible hybridization gap semiconductor. *Phys. Rev. B Condens. Matter Mater. Phys.* **91**, 085128 (2015).
21. M. E. Fisher, Relation between the specific heat and susceptibility of an antiferromagnet. *Philos. Mag.* **7**, 1731–1743 (1962).
22. S. L. Brock, J. E. Greedan, S. M. Kauzlarich, A test of the application of extended Hückel calculations to the ThCr_2Si_2 and CaAl_2Si_2 structure types: The case of SrMn_2P_2 and BaMn_2P_2 . *J. Solid State Chem.* **109**, 416–418 (1994).
23. N. D. Mermin, H. Wagner, Absence of ferromagnetism or antiferromagnetism in one- or two-dimensional isotropic Heisenberg models. *Phys. Rev. Lett.* **17**, 1133–1136 (1966).
24. H. Obara, Y. Endoh, Y. Ishikawa, T. Komatsubara, Magnetic phase transition of MnP under magnetic field. *J. Phys. Soc. Jpn.* **49**, 928–935 (1980).
25. D. C. Johnston, Magnetic susceptibility of collinear and noncollinear Heisenberg antiferromagnets. *Phys. Rev. Lett.* **109**, 077201 (2012).
26. D. C. Johnston, Unified molecular field theory for collinear and noncollinear Heisenberg antiferromagnets. *Phys. Rev. B Condens. Matter Mater. Phys.* **91**, 064427 (2015).
27. R. Nath *et al.*, Single-crystal ^{31}P NMR studies of the frustrated square-lattice compound $\text{Pb}_2(\text{VO})(\text{PO}_4)_2$. *Phys. Rev. B Condens. Matter Mater. Phys.* **80**, 214430 (2009).
28. N. Higa *et al.*, NMR studies of the incommensurate helical antiferromagnet EuCo_2P_2 : Determination of antiferromagnetic propagation vector. *Phys. Rev. B* **96**, 024405 (2017).
29. Q. P. Ding, N. Higa, N. S. Sangeetha, D. C. Johnston, Y. Furukawa, NMR determination of an incommensurate helical antiferromagnetic structure in EuCo_2As_2 . *Phys. Rev. B* **95**, 184404 (2017).
30. R. Navarro, J. J. Smit, L. J. De Jongh, W. J. Crama, D. J. W. Ijdo, Experimental and theoretical study of the antiferromagnetic double-layer compounds $\text{Rb}_3\text{Mn}_2\text{F}_7$ and $\text{K}_3\text{Mn}_2\text{F}_7$. *Phys. B+C* **83**, 97–116 (1976).
31. D. Beeman, P. Pincus, Nuclear spin-lattice relaxation in magnetic insulators. *Phys. Rev.* **166**, 359–375 (1968).
32. T. Moriya, The effect of electron-electron interaction on the nuclear spin relaxation in metals. *J. Phys. Soc. Jpn.* **18**, 516–520 (1963).
33. J. M. Hastings, L. M. Corliss, First-order antiferromagnetic phase transition in MnS_2 . *Phys. Rev. B* **14**, 1995–1996 (1976).
34. T. Chattopadhyay, H. G. von Schnering, H. A. Graf, First order antiferromagnetic phase transition in MnS_2 . *Solid State Commun.* **50**, 865–867 (1984).
35. B. C. Frazer, G. Shirane, D. E. Cox, C. E. Olsen, Neutron-diffraction study of antiferromagnetism in UO_2 . *Phys. Rev.* **140**, A1448–A1452 (1965).
36. C. G. Shull, W. A. Strauser, E. O. Wollan, Neutron diffraction by paramagnetic and antiferromagnetic substances. *Phys. Rev.* **83**, 333–345 (1951).
37. D. Bloch, R. Maury, C. Vetter, W. B. Yelon, Order-parameter and the discontinuous antiferro-paramagnetic transition in manganese oxide. *Phys. Lett. A* **49**, 354–356 (1974).
38. P. Bak, S. S. Krinsky, D. Mukamel, First-order transitions, symmetry, and the ϵ expansion. *Phys. Rev. Lett.* **36**, 52–55 (1976).
39. D. Mukamel, S. Krinsky, Physical realizations of the $n \geq 4$ -component vector models. I. Derivation of the Landau-Ginzburg-Wilson Hamiltonians. *Phys. Rev. B* **13**, 5065–5077 (1976).
40. D. Mukamel, S. Krinsky, Physical realizations of the $n \geq 4$ -component vector models. II. ϵ -Expansion analysis of the critical behavior. *Phys. Rev. B* **13**, 5078–5085 (1976).
41. P. Bak, D. Mukamel, Physical realizations of the $n \geq 4$ -component vector models. III. Phase transitions in Cr, Eu, MnS_2 , Ho, Dy, and Tb. *Phys. Rev. B* **13**, 5086–5094 (1976).
42. L. Zu *et al.*, A first-order antiferromagnetic-paramagnetic transition induced by structural transition in GeNCr_3 . *Appl. Phys. Lett.* **108**, 031906 (2016).